Space Weather

RESEARCH ARTICLE
10.1029/2022SW003132

Key Points:

- Phase scintillation is more severe than the amplitude scintillation at high-latitudes during the great storm
- The degraded positioning accuracy at high-latitudes is related to the large number of falsely detected cycle slip (CS) satellites
- Precise positioning can be achieved at high-latitudes under the geomagnetic storm, given that the CS problems are well addressed

Correspondence to:
T. Xu,
thxu@sdu.edu.cn

Citation:
Nie, W., Rovira-Garcia, A., Li, M., Fang, Z., Wang, Y., Zheng, D., & Xu, T. (2022). The mechanism for GNSS-based kinematic positioning degradation at high-latitudes under the March 2015 great storm. *Space Weather*, *20*, e2022SW003132. https://doi.org/10.1029/2022SW003132

Received 22 APR 2022
Accepted 12 JUN 2022

Author Contributions:
Conceptualization: Wenfeng Nie
Formal analysis: Adrià Rovira-Garcia
Investigation: Adrià Rovira-Garcia
Methodology: Wenfeng Nie
Resources: Yong Wang
Software: Mowen Li
Validation: Zhenlong Fang
Writing – original draft: Wenfeng Nie
Writing – review & editing: Wenfeng Nie

The Mechanism for GNSS-Based Kinematic Positioning Degradation at High-Latitudes Under the March 2015 Great Storm

Wenfeng Nie[1,2], Adrià Rovira-Garcia[3], Mowen Li[1,3], Zhenlong Fang[1], Yong Wang[1], Dunyong Zheng[4], and Tianhe Xu[1]

[1]Institute of Space Sciences, Shandong University, Weihai, China, [2]State Key Laboratory of Geo-information Engineering, Xi'an, China, [3]Research Group of Astronomy and Geomatics (gAGE), Universitat Politecnica de Catalunya (UPC), Barcelona, Spain, [4]National-Local Joint Engineering Laboratory of Geo-Spatial Information Technology, Hunan University of Science and Technology, Xiangtan, China

Abstract In this study, we focus on the kinematic precise point positioning (PPP) solutions at high-latitudes during the March 2015 great geomagnetic storm. We aim to discover the mechanism behind the positioning degradation from the perspective of the impacts of the storm-induced ionospheric disturbance on the global navigation satellite system (GNSS) data processing. We observed that the phase scintillation dominated the amplitude scintillation at high-latitudes and the variation pattern of the rate of total electron content index (ROTI) was consistent with that of the phase scintillation during the storm. The kinematic PPP errors at high-latitudes were almost three times larger than those at the middle- and low-latitude, which were accompanied by large ROTI variations. From the perspective of GNSS data processing, the large positioning errors were also found to be related to the large number of satellites experiencing cycle slips (CSs). Based on the lock time from the ionospheric scintillation monitoring receiver, we found that a large amount of the CSs was falsely detected under the conventional threshold of the CS detector. By increasing such threshold, the kinematic positioning accuracy at high-latitudes can be improved to obtain similar magnitude as at middle- and low-latitude. The improved positioning accuracy may suggest that the ionospheric disturbance induced by the geomagnetic storm at high-latitudes has minor effects on triggering the CSs. Therefore, precise positioning can be achieved at high-latitudes under geomagnetic storms, given that the CS problem is well addressed.

Plain Language Summary Geomagnetic storm is one kind of extreme space weather events, which disturbs the radio communication and degrade the precision of the global navigation satellite system (GNSS). Much efforts have been made to study the ionospheric responses to different geomagnetic storms and its impact on the GNSS performances. During intense geomagnetic storms, the positioning accuracies for stations at high-, middle- and low-latitudes are likely to degrade. Particularly, the positioning errors are more severe for stations at high-latitudes due to the more frequent cycle slip (CS) than those at middle- and low-latitudes under the same storm. In this study, we found that the degraded positioning accuracy at high-latitudes was not only related to the large rate of total electron content index (ROTI) variation but also to the large number of the CS. Particularly, we deduce that a large amount of the CSs was falsely detected under the conventional threshold of the CS detector. The results in the study suggest that the ionospheric disturbance induced by the geomagnetic storm at high-latitudes has minor effects on triggering the CSs. Therefore, precise positioning can be achieved at high-latitudes under the geomagnetic storm, as long as the CSs can be well addressed.

1. Introduction

Geomagnetic storms are large perturbations of the Earth's space environment. Such perturbations result from solar eruptions such as solar flares and coronal mass ejections followed by its transit from the Sun to the Earth and the subsequent coupling of its energy and mass to the magnetospheric-ionospheric-thermospheric domain (Kamide et al., 1997). Stronger geomagnetic disturbances usually trigger ionospheric storms, that is, the enhancements or depletions of the ionospheric electron density. The knowledge of ionospheric irregularities has practical significance for such areas of human activity as positioning, navigation, and timing using global navigation satellite systems (GNSS), and other applications related with space weather (Förster & Jakowski, 2000).

The ionospheric irregularities can adversely impact the performance of GNSS through the mechanism of the refractive and diffractive effects (Basu et al., 2002; Knight & Finn, 1998). The refractive effects on trans-ionospheric radio waves are well-known as ranging errors, having a well-established relationship with the electron density along the raypath and the frequency of the wave. On the other hand, the diffractive effects are known to be observed as rapid fluctuations in the signal's amplitude and phase, referred to as scintillation (Kintner et al., 2007; McCaffrey & Jayachandran, 2019). The ionospheric scintillation affects the GNSS performance by increasing the noise of the observations and reducing the receiver signal tracking performance (Knight & Finn, 1998). In the case of phase scintillation, diffraction induces rapid phase shifts, which may exceed the receiver phase lock loop bandwidth, resulting in phase loss of lock (LoL) (Skone et al., 2001; Sreeja et al., 2011). In contrast, amplitude scintillation reduces the signal-to-noise ratio and when the depth of such fading exceeds the fade threshold of the GNSS receiver, signal loss and cycle slip (CS) occur (Skone et al., 2005).

Much efforts have been made to study the impact of the ionospheric irregularities triggered by geomagnetic storms on the GNSS precise positioning. Afraimovich et al. (2003) investigated the degradation of global positioning system (GPS) performance in middle-latitude region under geomagnetically disturbed conditions. It was found that magnetic storm conditions were accompanied by an increase in the spherical standard deviation of the position errors obtained by the GPS receivers. Focusing on the positioning performance at low-latitudes under such storms, Lu et al. (2020) and Zakharenkova and Cherniak (2021) found the dual-frequency GPS-based positioning accuracy degraded at many permanent stations located from low-to middle-latitudes in Hong Kong and North America, affected by the transported storm-induced plasma depletions and associated irregularities. Luo et al. (2018) presented the performance dual-frequency and single-frequency precise point positioning (PPP) with GPS under moderate, intense, and super storm conditions during solar cycle 24 using a large data set collected from about 500 stations belonging to the International GNSS Service (IGS). The global root mean square (RMS) maps of GPS PPP results showed that stations with degraded performance were mainly distributed at high-latitudes, and the degradation level generally depended on the storm intensity. In addition, it was found that the degraded performance of GPS positioning during geomagnetic storms increased with the severity of ionospheric disturbances, which not only lead to the deteriorated ionospheric correction but also to the more frequent CS occurrence. Yang et al. (2020) presented the first results of storm-induced ionospheric disturbance impacts on kinematic GPS PPP solutions during the geomagnetic storm of 17–18 March 2015 by taking advantage of over 5,500 stations installed worldwide. The results showed that the overall impact was more severe at high-latitudes, while PPP degradation at low-latitudes was associated with different types of ionospheric disturbances. Specifically, the PPP degradation at high-latitudes was associated with intense ionospheric plasma irregularities and storm enhanced density/tongue of ionization structures while that at low-latitudes was related to the penetration electric field-induced post-sunset equatorial plasma irregularities and the equatorial ionosphere anomalies. In summary, past researchers showed that under geomagnetic storms, positioning accuracies for stations in high-, middle- and low-latitude region are likely to degrade. In addition, the positioning errors are more severe for stations at high-latitudes due to the more frequent CS than those at low-latitudes under the same storm.

However, Juan, Sanz, González-Casado et al., 2018 pointed out that at high-latitudes, PPP can be achieved during the strong scintillation conditions. In this region the size of the irregularities is typically larger than the Fresnel length, so the main effects on the GNSS signals were related with the fast change on the refractive index associated to the fast movement of the ionospheric irregularities. Consequently, the main effect on the GNSS signals was a fast fluctuation of the carrier phase, but with a moderate fade in the amplitude. Therefore, the ionospheric fluctuations at high-latitudes usually did not produce CSs, being the effect quite limited on the ionosphere-free (IF) combination. The discrepancy between Juan, Sanz, González-Casado et al., 2018 and the aforementioned references motivated us to further discover the mechanism of the positioning degradation at high-latitudes during geomagnetic storms.

The St. Patrick's storm on 17 March 2015 was the strongest during the 24 solar cycle. A considerable number of researchers have investigated the ionospheric disturbances as well as the GPS positioning performance associated with the great storm (Cherniak & Zakharenkova, 2015; Cherniak et al., 2015; Jacobsen & Andalsvik, 2016; Jin et al., 2017, 2019; Liu et al., 2016; Mansilla, 2019; Nava et al., 2016; Poniatowski & Nykiel, 2020; Prikryl et al., 2016; Prol et al., 2021; Yao et al., 2016; Zakharenkova et al., 2016, 2019). Particularly, Yang et al. (2020) conducted a comprehensive accuracy assessment of the kinematic PPP using more than 5,000 stations around the world, focusing on the relationship between the positioning degradation and the ionospheric plasma irregularities

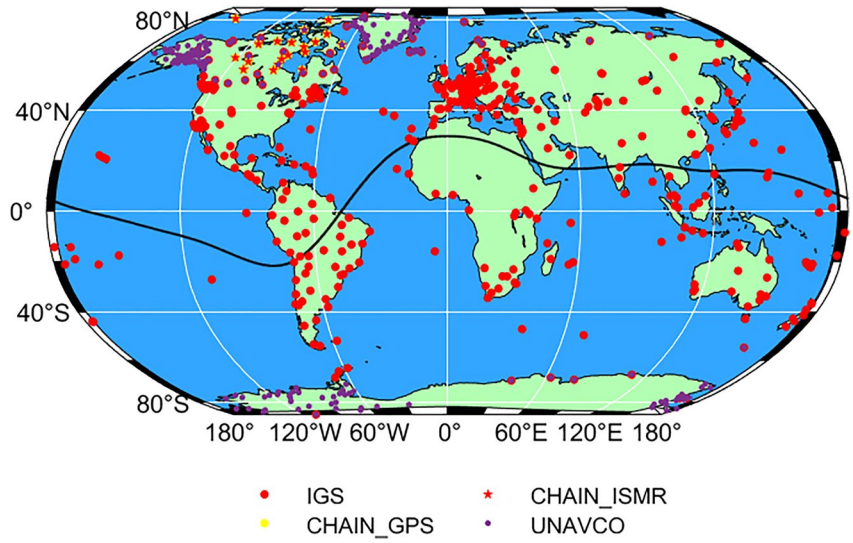

Figure 1. Worldwide distribution of the used permanent stations. The black solid line indicates the magnetic equator. The red dots represent stations from International GNSS Service, red stars and yellow dots represent ionospheric scintillation monitoring receiver and global positioning system stations from Canadian High Arctic Ionospheric Network, and purple dots represent stations from University NAVSTAR Consortium.

in different regions on the globe. Different from the perspective of Yang et al. (2020), we try to discover the reason behind the positioning accuracy degradation at high-latitudes from the aspect of the impacts of the storm-induced ionospheric disturbance on GNSS data processing, especially the impacts of CSs.

2. Data and Methodology

2.1. GPS Data

GPS data at a sampling rate of 30 s from more than 750 permanent stations were processed for addressing the ionospheric disturbance effects on GPS kinematic positioning solutions on 17 March 2015. Among them, about 500 stations that distributed around the world belong to the IGS network and about 200 stations with absolute magnetic latitude, $|\varnothing_m|$, greater than 60° belong to the network of University NAVSTAR Consortium (UNAVCO). Particularly, we select 19 GPS stations from the Canadian High Arctic Ionospheric Network (CHAIN), which can operate as dual-band GNSS receivers as well as ionospheric scintillation monitoring receiver (ISMR). According to the magnetic latitude distribution, the high-latitude can be defined as $|\varnothing_m| > 60°$, the middle-latitude as $20° < |\varnothing_m| \leq 60°$, and the low-latitude as $|\varnothing_m| < 20°$. Therefore, a total number of 300 stations are located at high-latitudes in the study. The distribution of the permanent stations is presented in Figure 1.

2.2. Magnetic Storm and Ionospheric Disturbance Index

In order to evaluate the level of magnetic activity during the 2015 St. Patrick's Day storm, we used the magnetic storm index, including the interplanetary magnetic field (IMF) components, the longitudinally symmetric disturbances index in the horizontal direction (SYM-H), and auroral electrojet (AE) indices. Besides, the solar wind speed and pressure parameters were obtained to assess the effect from the solar activity.

To measure ionospheric disturbances at the same stations presented in Figure 1, we used the rate of total electron content index (ROTI) metrics derived from GPS dual-frequency carrier-phase measurements. The ROTI is defined as the standard deviation of the rate of total electron content (TEC) and an indicator generally used for quantifying small-scale ionospheric plasma irregularities (Pi et al., 1997). These disturbances are expected to generate significant scintillation effects on GNSS signals, in such a way that ROTI values can be related with the impacts on kinematic PPP solutions throughout our analysis. We computed the ROTI every 5 min with data sampled every 30 s.

Table 1
Summary of Data Processing Techniques Used in Our Study

Item	Techniques and implementations
Observations	GPS dual-frequency code and phase measurements
Processing mode	Forward
Sampling interval	30 s
Elevation mask angle	7°
Cycle-slip detection	Phase Geometry-free and Hatch-Melbourne-Wubbena combination
Satellite orbit and clock	Fixed with the final products from IGS with an interval of 15 min (orbit) and 5 min (clock)
Phase center offset	igs08.atx
Ionospheric delay	First-order effect eliminated by ionospheric-free linear combination
Differential Code Bias	Corrected by P1C1 DCBs from Center for Orbit determination in Europe
Tropospheric delay	The Saastamoinen model for the initial zenith dry and wet delay (Saastamoinen, 1972), along with the GMF projection function (Boehm et al., 2006), and the wet delay is estimated as constant every 2 hr
Solid earth tide, ocean tide loading, and pole tide	IERS Conventions 2010 (Petit & Luzum, 2010); FES2004 (Lyard et al., 2006) for ocean tides
Relativity effect	IERS Conventions 2010

In addition, we used several ISMRs from the CHAIN in the study. The ISMR can provide amplitude scintillation index S4 and phase scintillation index σ_φ. S4 can be calculated from the satellite signal power or signal intensity tracked by the receiver, as a normalized standard deviation around the intensity average. The phase scintillation index σ_φ is characterized by the standard deviation φ of the detrended phase (Van Dierendonck et al., 1993). The S4 and σ_φ indexes from CHAIN are provided with an interval of 60 s; the scintillation level can be classified as weak when $0.3 \leq S4 < 0.4$; moderate when $0.4 \leq S4 < 0.7$; and strong when $S4 \geq 0.7$ (Series, 2012; Sreeja et al., 2020).

2.3. GPS Kinematic Positioning Algorithms

The GPS carrier phase and pseudorange measurements were processed as kinematic PPP solutions by utilizing routines from the Real-Time Kinematic Library (RTKLIB) (Takasu, 2013). In our study, the kinematic positions of the globally distributed GPS receivers were computed every 30 s. An elevation cut-off angle of 7° was used to reduce the multipath effects on the position calculation while that of 20° was adopted to avoid the geometrical effects as well as the multipath effects on the ROTI calculations (Juan, Sanz, Rovira-Garcia et al., 2018; Pi et al., 1997). The detailed data processing techniques and implementations for GPS dual-frequency PPP are summarized in Table 1.

Under normal conditions and after a convergence period of about one hour, the kinematic PPP can achieve decimeter-level accuracy for the receiver with the above processing strategy. In our study, the kinematic PPP solutions were evaluated by a comparison with their daily solutions in static PPP mode on 16 March 2015; that is, one day before the storm. The position errors were further examined in association with the storm-induced ionospheric disturbances.

2.4. Cycle Slip Detection Algorithm

The performance of algorithms to detect CSs, that is, discontinuities on the carrier-phase measurements, is critical for the positioning accuracy and stability when extreme space weather events occur. Though many CS detection algorithms have been proposed over the past decades, the TurboEdit algorithm is maybe the most widely used in GNSS data processing (Blewitt, 1990). Indeed, popular GNSS data processing software, such as GIPSY, Bernese, PANDA as well as the RTKLIB package used in this study, adopt the TurboEdit algorithm or algorithms based on TurboEdit (Bertiger et al., 2020; Dach et al., 2015; Liu & Ge, 2003). The TurboEdit algorithm is based on the

Hatch–Melbourne-Wübbena (HMW) and Phase-Geometry-Free (PGF) combination observables (Hatch, 1983; Melbourne, 1985; Wubbena, 1985). The two basic CS detectors can be written as follows:

$$\Delta N_{HMW} = \Delta\varphi_1 - \Delta\varphi_2 - \frac{f_1\Delta P_1 + f_2\Delta P_2}{\lambda_{HMW}(f_1 + f_2)} + \Delta\xi_{\mathrm{HMW}}$$
$$\Delta\varphi_{\mathrm{PGF}} = \lambda_1\Delta\varphi_1 - \lambda_2\Delta\varphi_2 = \lambda_1\Delta N_1 - \lambda_2\Delta N_2 + (\gamma - 1)\Delta I + \Delta\xi_{\mathrm{PGF}} \quad (1)$$

where Δ is the difference operator between two consecutive epochs which are separated 30 s in the present study; P_j in the unit of meter and φ_j in the unit of cycle are the pseudorange and carrier phase at the frequency j; j equals to 1 and 2, standing for the GPS L1 and L2 band signal; f_j, λ_j, and N_j are the corresponding frequency, wavelength, and integer ambiguity parameters; $\lambda_{HMW}$is the wide-lane wavelength of 86 cm; γ is the frequency-dependent multiplier factor with $\gamma = (f_1/f_2)^2$; ΔI is the epoch-wise variation of the ionosphere delay at the L1 band; $\Delta\xi$ is the unmodelled noise from the wind-up effect, the phase center offsets, and variations in the combined observables.

For the TurboEdit algorithm, the commonly used threshold for the HMW observable is from 1 to 2 cycles of HMW (where 1 cycle accounts for 86 cm), while the customary threshold for the PGF observable ranges from 0.05 to 0.15 m (Zhang et al., 2014). The RTKLIB package used in the present study, sets as default threshold of the PGF observable to 0.05 m (Takasu, 2013). We will show in the Results and Discussion section that, with the default thresholds, the kinematic PPP can achieve accurate and stable performance under ionospheric quiet conditions.

3. Overview of Magnetic Storm and Ionospheric Disturbance Conditions

Figure 2 shows the variations of the interplanetary and geomagnetic parameters during 16–18 March, 2015. On the quiet day of 16 March 2015, the magnetic activity was weak with the IMF Bz directing northward most of the time. The solar wind speed increased gradually from 300 km/s to about 430 km/s during the day, and solar wind dynamic pressure was mostly less than 10 nPa.

The storm sudden commencement (SSC) was registered at 04:45 UT on 17 March 2015. The solar wind speed and the dynamic pressure that was recorded by the Advanced Composition Explorer (ACE) experienced a sudden increase from 400 km/s to over 500 km/s, and from approximately 5 nPa to over 30 nPa, respectively. The main phase of the geomagnetic storm was triggered by a fast southward turning of IMF Bz with large negative values of about −20 nT at around 06:00 UT on 17 March 2015. The solar wind speed (∼600 km/s) and pressure (13–25 nPa) increased significantly relative to the quiet previous days. AE reached its first peak value of 981 nT at ∼08:50 UT, and another peak appeared at 13:55 UT. Meanwhile, the SYM-H index attained a minimum value of −233 nT at 22:45 UT. Then the recovery phase started around 23:00 UT.

On 18 March 2015 and later days, the solar wind speed maintained a relatively large value ranging from 450 km/s to 700 km/s but dynamic pressure returned to its quiet time level. In addition, IMF Bz fluctuated between northward and southward with a magnitude of around 5 nT.

To assess the ionospheric disturbance conditions, we present the amplitude scintillation, phase scintillation, together with the corresponding ROTIs indices of four selected stations from the CHAIN in Figure 3. The ionospheric condition before the day of the great storm, that is 16 March 2015, is also presented for comparison.

From Figure 3, we can see that the ionospheric variation for the four stations was similar during 16–17 March, 2015. One key feature we can find from Figure 3 is that the phase scintillation was more severe than the amplitude scintillation for the selected stations at high-latitudes. This feature is caused by the nature of the ionospheric irregularities that the amplitude scintillation occurrence in the polar region was very low (Basu et al., 1985; Prikryl et al., 2010). In addition, we can find that the variation pattern of ROTI was similar to that of the phase scintillation for all of the four stations, indicating the effectiveness of the ROTI to describe the ionospheric disturbance at high-latitudes. At last, from the point of the phase scintillation and ROTI indices, the ionospheric condition on 17 March 2015 was more disturbed than that on 16 March 2015, suggesting the effects of the geomagnetic storm on the ionosphere.

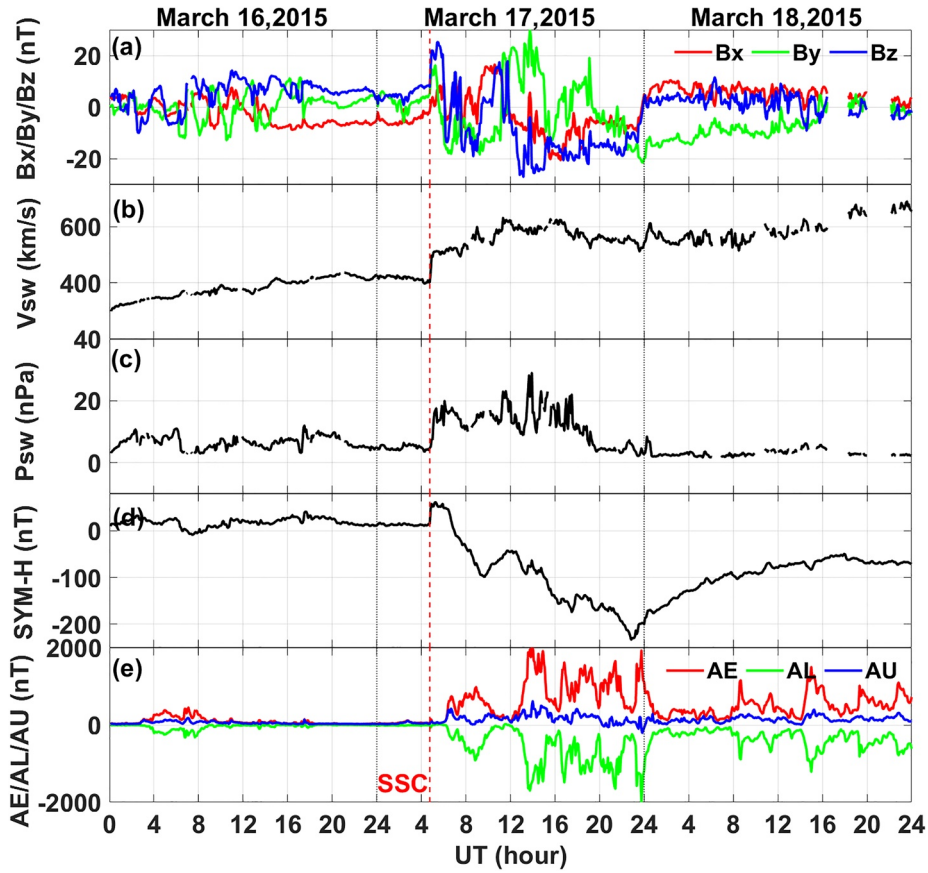

Figure 2. Variations of geomagnetic conditions during 16–18 March, 2015. (a) The interplanetary magnetic field Bx, By, and Bz components; (b) velocity of the solar wind; (c) pressure of the solar wind; (d) the geomagnetic symmetric disturbances index in the horizontal direction index; (e) auroral electrojet AE/AL/AU indices.

To describe the ionospheric variation on a global scale, we calculated the ROTI at the 700 stations. Thus, Figure 4 depicts the global temporal-spatial variations of ROTI as a function of geographic longitude and latitude, from 16 March to 17 March 2015. Since the ROTI is calculated at a 30 s rate over 5 min, the time title above the subfigures identifies the start time of the window computing the ROTI.

From Figure 4, we can see that the ROTIs at high-latitudes, including the north hemisphere and south hemisphere, were usually larger than those in middle- and low-latitude region. During the pre-storm period (before 04:00 UT), most of the ROTIs at high-latitudes were around 0.4 TECU/min while those in the other regions were below 0.2 TECU/min. Combining with Figure 3, we can find that ROTIs increased from about 08:00 UT. From Figure 4, we can find that many of the ROTIs increased to the magnitude larger than 1.0 TECU/min at high-latitudes from 10:00 UT. Thus, after the SSC of the geomagnetic storm (04:45 UT), the increased geomagnetic activity led to ionospheric disturbances of various types, scales, and geographical location.

4. Results and Discussions

In this section, the global kinematic PPP performance during the storm is first presented with focus on the positioning errors at high-latitudes. Then, we turn our attention to the reason behind the positioning accuracy degradation.

4.1. Kinematic Precise Point Positioning Performance During the Storm

We conducted the kinematic PPP solutions according to the strategy summarized in Table 1. The distribution of the 3-Dimension (3D) PPP errors is presented in Figure 5. Since the sampling rate of the GPS data was 30 s,

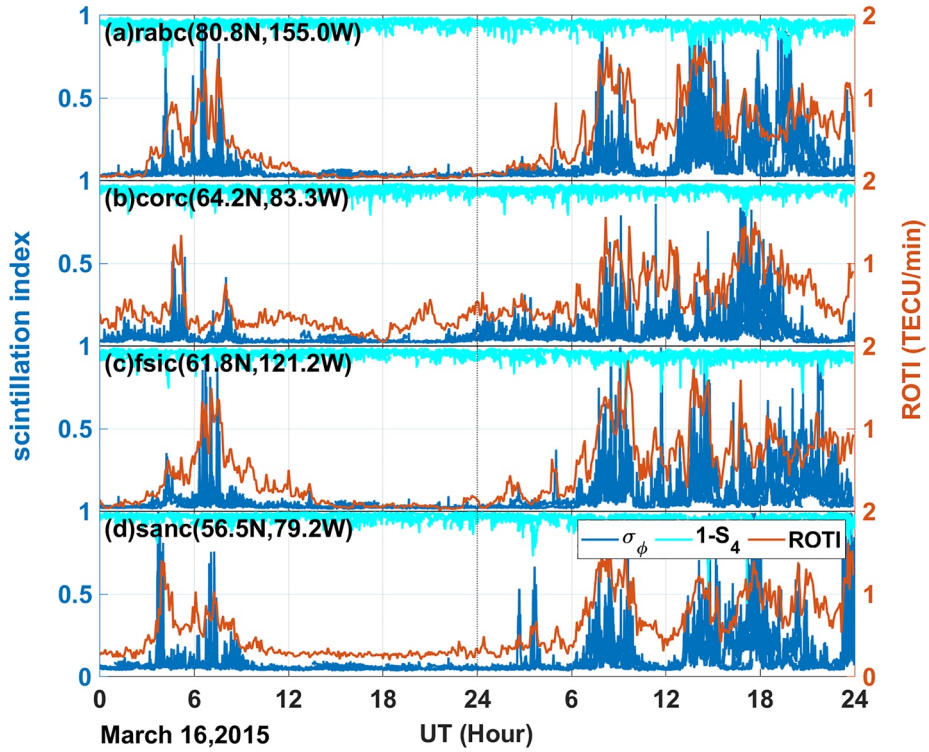

Figure 3. Global positioning system amplitude and phase scintillation index and corresponding rate of total electron content index for four selected stations belonging to Canadian High Arctic Ionospheric Network during 16–17 March, 2015.

we computed the RMS of the positioning errors every 5 min to match the ROTI analysis. The time description above the subfigures in Figure 5 indicates the start time of the 5 min window to compute the 3D RMS of the positioning errors. Besides, the time of the snapshots in Figure 5 is consistent with that in Figure 4 to have a direct comparison.

From Figure 5, we can find that the magnitude distribution of the kinematic 3D PPP errors was basically consistent with the magnitude distribution of the ROTIs. We can see that the 3D PPP errors of most of the stations were around 0.2 m before the geomagnetic storm (before 04:45 UT). However, we can see notable degradations of the PPP errors, which can even exceed more than 1.0 m, from the snapshot after 10:00 UT. More importantly, we can see that the large kinematic PPP errors mostly occurred at high-latitudes, indicating that the accuracy of the kinematic PPP at high-latitudes was more affected by the geomagnetic storm than that in other regions. This phenomenon is consistent with the results from Luo et al. (2018) and Yang et al. (2020). In Yang et al. (2020), the kinematic PPP errors on 17 March 2015 were analyzed in more detail, focusing on the relationship between the positioning degradation and the ionospheric plasma irregularities in different regions on the globe.

We then quantified the horizontal and vertical positioning errors by separating the stations located at high-, middle- and low-latitudes. There are about 300 stations located at high-latitudes, 350 stations located at middle-latitudes, and 60 stations located at low-latitudes. For comparison, the positioning errors on the geomagnetic-quiet day of 16 March 2015 are also presented in Figure 6 and Table 2. To reduce the impacts of the positioning errors during the initialization period on the accuracy statistics, the positioning errors in the first three hours on 16 March 2015 are not considered.

From Figure 6, we can see that the horizontal and vertical errors of the kinematic PPP solution in the different regions were quite stable on the geomagnetic quiet day of 16 March 2015. As shown in Table 2, the mean RMS in the horizontal and vertical component at high-latitudes was a bit larger than that in the other regions, as 9.0 and 10.8 cm, respectively. However, when it came to the geomagnetic disturbed day of 17 March 2015, the mean RMS in the horizontal and vertical component at high-latitudes increased to 24.0 and 36.1 cm, which was more than three times worse than the corresponding accuracy on 16 March 2015. In contrast, the accuracy in the horizontal

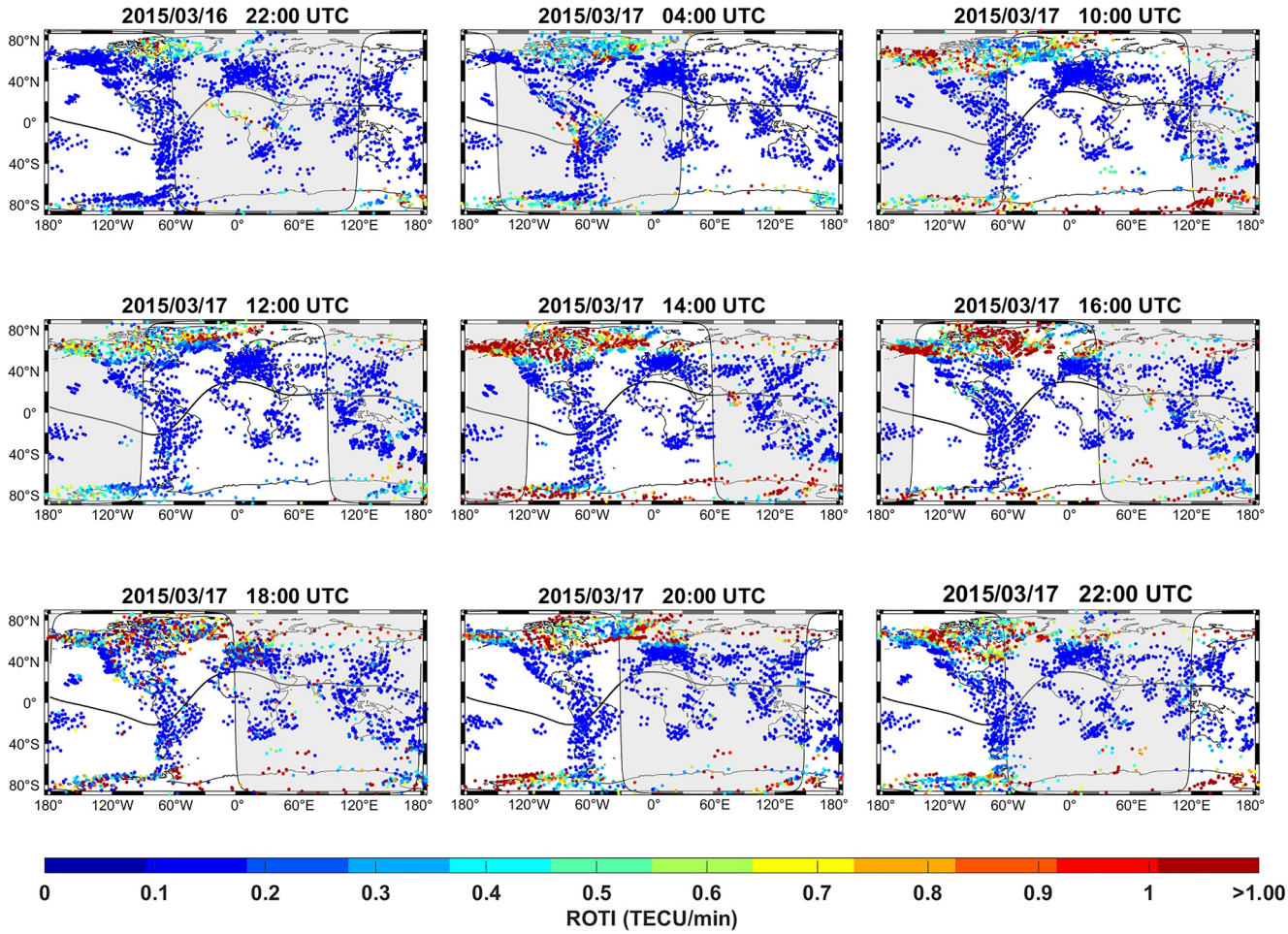

Figure 4. Snapshots of global temporal-spatial variations of rate of total electron content index during 16–17 March, 2015. The gray shade indicates the night side. The black solid line represents the magnetic equator.

and vertical component for the middle- and low-latitude region slightly decreased when the geomagnetic storm occurred on 17 March 2015.

In addition, comparing Figure 3 with Figure 6, we can find that the variation pattern of the phase scintillation and ROTI indices in Figure 3 was similar to that of the horizontal and vertical positioning errors at high-latitudes as presented in Figure 6(a). For example, when the phase scintillation/ROTI indices greatly fluctuated from about 08:00 UT on 17 March 2015 in Figure 3, we can see that both the horizontal and vertical errors increased almost simultaneously in Figure 6. In the previous research, the notable positioning accuracy degradation at high-latitudes during the geomagnetic storm was attributed to the significant ionospheric disturbance, as depicted by the phase scintillation or ROTI indices, at high-latitudes (Luo et al., 2018; Yang et al., 2020). In particular, Yang et al. (2020) made an overall summary on the physical mechanism behind the remarkable ROTI variation at high-latitudes, which was related to the storm-induced gradient of the plasma density caused by auroral particle precipitation and plasma flows. Different from the perspective of Yang et al. (2020), we try to discover the reason behind the positioning accuracy degradation from the aspect of the impacts of the storm-induced ionospheric disturbance on GNSS data processing in the following.

4.2. The Reason Behind the Kinematic PPP Accuracy Degradation

We select three stations at high-latitudes to display the detailed statistics from the GPS data processing. Station *CORC* is from CHAIN with ISMR observations and the other two stations, as *YELL* and *BACK*, are geodetic-grade receivers from IGS located at the north hemisphere and south hemisphere, respectively.

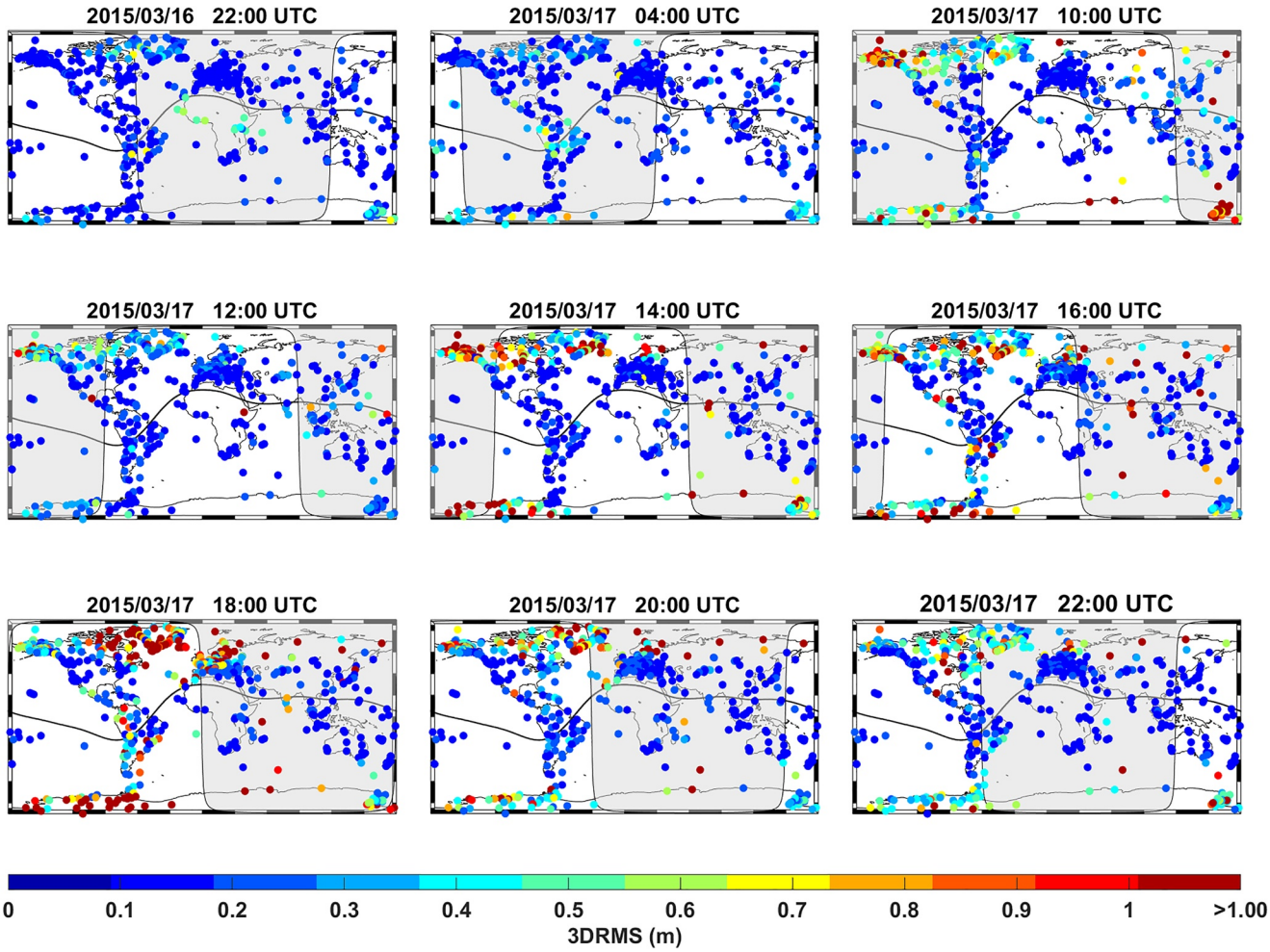

Figure 5. Snapshots of kinematic 3D precise point positioning errors on 16–17 March, 2015. The gray shade indicates the night side. The black solid line represents the magnetic equator.

Taking the results from station *CORC* as an example, we can see from Figure 7(a) that the maximum RMS in the horizontal and vertical component can reach 2 m. Comparing Figure 7(a) with 7(d), we can see that when the phase scintillation and ROTI indices increased around 08:00 UT, 12:00 UT, and 18:00 UT, the positioning RMS in the horizontal and vertical component increased correspondingly, indicating the effect of the disturbed ionosphere on the positioning accuracy.

We then turn our attention to the statistical details for the kinematic PPP solution. From Figure 7(g), we can see that the number of the tracked and used satellites varies from 8 to 12. Most of the time, the position dilution of precision (PDOP) of the kinematic PPP solution keeps stable around 2, although there existed some fluctuations for some epochs. Around 08:00 UT, the number of used satellites was above 10 while the PDOP value was below 2, indicating a strong satellite geometry. However, as it can be seen in Figure 7(a), the positioning accuracy at around 08:00 UT decreased dramatically. Therefore, the positioning accuracy degradation cannot be attributed to a bad geometry of the observed satellites. In fact, comparing Figure 7(g) with 7(a), we can also see that the number of CS satellites increased dramatically at around 08:00 UT, 12:00 UT, and 18:00 UT, at the time of which the positioning RMS error in the horizontal and vertical component increased. In other words, the positioning RMS in the horizontal and vertical component may be not only related to the phase scintillation and ROTI indices, but also to the number of the CSs affecting multiple satellites.

In the case of stations *YELL* and *BACK*, as shown in the middle and right columns of Figure 7, we can see a similar performance of the positioning RMS with regard to the phase scintillation and ROTI indices, as well as

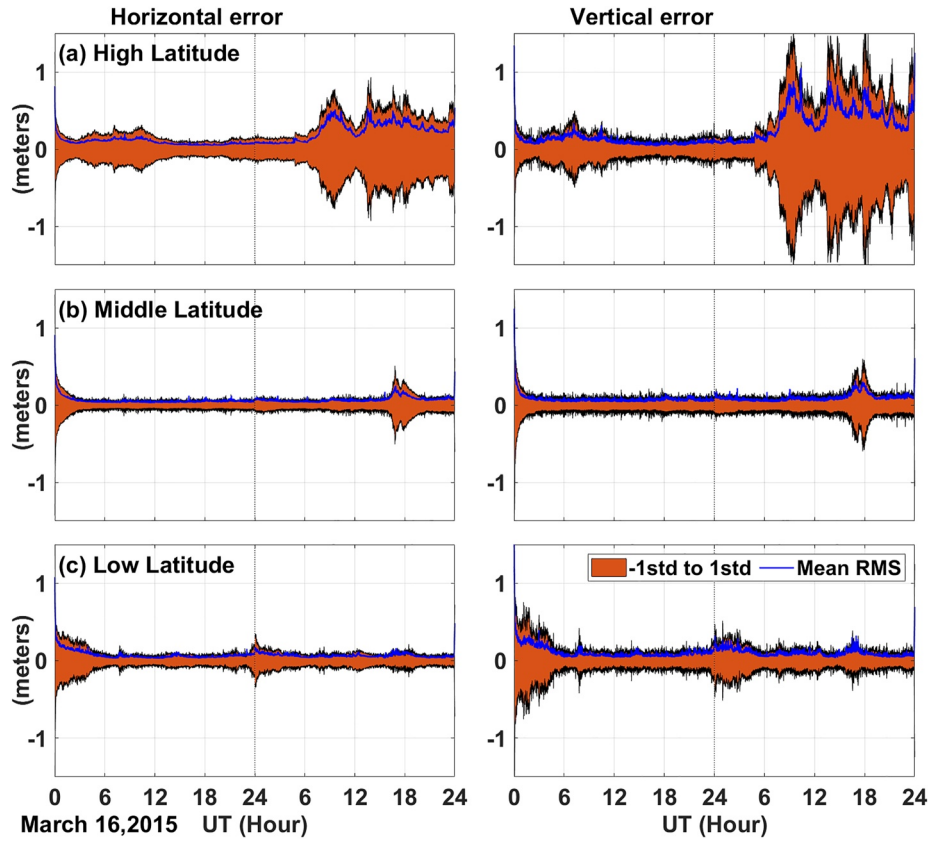

Figure 6. Horizontal (left column) and vertical (right column) errors of kinematic precise point positioning solutions for (a) high-latitudes; (b) middle-latitudes; (c) low-latitudes on 16–17 March, 2015. The orange area and solid blue lines represent one-standard-error bands and mean root mean square of the solution errors, respectively.

the number of the satellites experiencing CSs. For example, the positioning error in the horizontal and vertical component for the station *YELL* reached a maximum around 10:00 and 14:00 UT in Figure 7(b); meanwhile, we can see peaks at around 10:00 and 14:00 UT for both the ROTI and the number of CS satellites in Figure 7(e) and 7(h). Since the occurrence of the remarkable ROTIs at high-latitudes with regard to the different scale plasmas irregularities has been analyzed in detail in Yang et al. (2020), we focus on the impacts of the number of satellites affected by CS on the positioning degradation from the perspective of GNSS data processing.

To further discover the relationship between the positioning accuracy and the number of CS affecting GNSS satellites, Figure 8 presents the occurrence rate of the CS satellites for over 700 stations on a global scale on 16–17 March, 2015.

As it can be seen from Figure 8, the occurrence rate of the CS satellites for most of the stations on the geomagnetic storm day of 17 March 2015 was higher than that in 16 March 2015. Particularly, the occurrence rate of the CS at high-latitudes was larger than that in the other regions. Comparing Figure 8 with Figures 4 and Figure 5,

Table 2
Statistics of the Positioning Accuracy in Different Region on 16–17 March, 2015

	Mean RMS (cm) 16 March 2015		Mean RMS (cm) 17 March 2015	
Geomagnetic latitude	Horizontal	Vertical	Horizontal	Vertical
High	9.0	10.8	24.0	36.1
Middle	4.9	6.9	7.4	10.0
Low	6.1	9.0	6.8	10.2

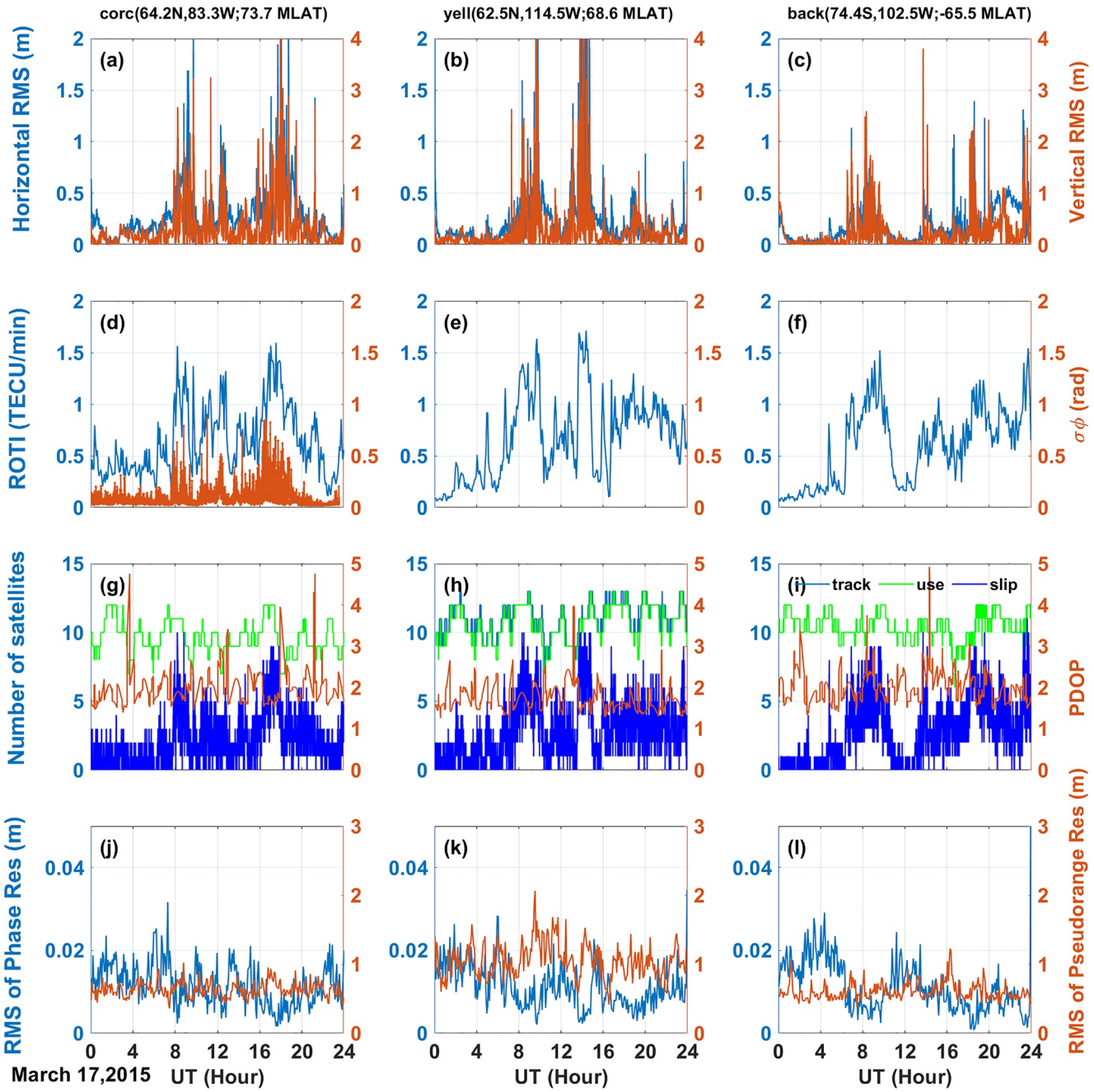

Figure 7. The kinematic precise point positioning (PPP) for stations *CORC* (left column), *YELL* (middle column), and *BACK* (right column) on 17 March 2015 under the threshold of 0.05 m for Phase-Geometry-Free combination. (a)–(c) presented the horizontal and vertical positioning accuracy; (d)–(f) presented the rate of total electron content index and phase scintillation indices; (g)–(i) presented the number of the tracked satellites, the used satellites, the satellites with cycle slips, as well as the position dilution of precision information of the PPP solution (j)–(l) presented the 5-min root mean square of the carrier-phase and pseudorange residuals of the kinematic PPP solutions.

we can find that the magnitude distribution of the CS occurrence rate was consistent with that of the positioning error and ROTI. In order to quantify the increase in the CS occurrence rate, we computed the mean occurrence rate of the CS satellites for stations in the different regions. As a result, the mean occurrence rate of the CS satellites in high-, middle- and low-latitude regions on 16 March 2015 are 15.0%, 14.7%, and 19.6%, respectively. In comparison, the mean occurrence rate of the CS satellites on 17 March 2015 at high-latitudes is 30.6% while that

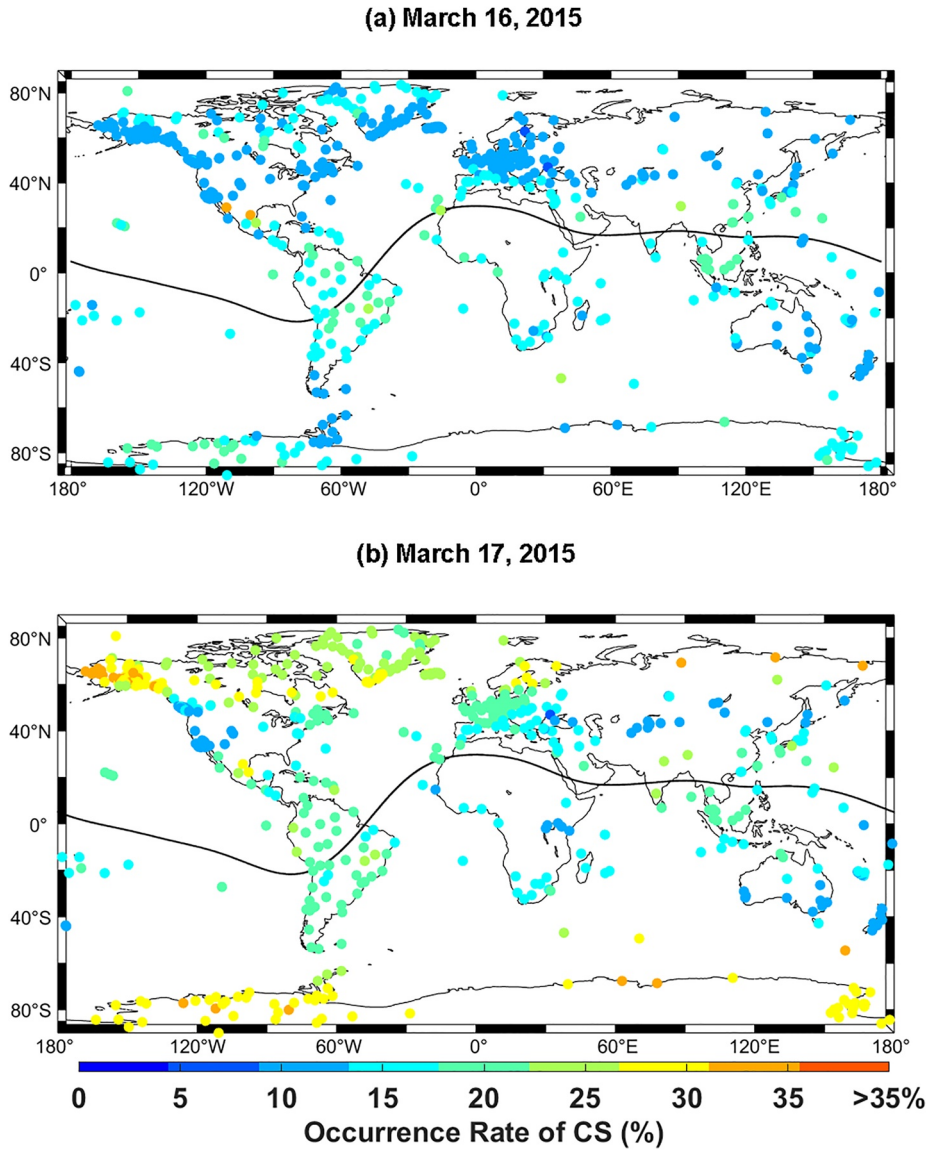

Figure 8. Cycle slip occurrence rate for over 700 stations around the world on March 16 (top plot) and 17 (bottom plot), 2015.

is 18.4% and 20.3% in middle- and low-latitude region. Therefore, stations at high-latitudes on 17 March 2015 are more affected by the CS satellites.

In PPP processing, once CSs are detected, the Kalman filter re-initializes the estimation of the carrier-phase ambiguities by increasing the process noise of the estimation and multiplying by zero the last estimated value. In essence, the Kalman filter "forgets" about the previous ambiguity estimate for that satellite and starts estimating the new ambiguity, which will be a constant value until a new CS occurs. When multiple CSs are detected simultaneously, the number of such unknown parameters increases. Therefore, the redundancy of observations decreases, ultimately reducing the carrier phase residuals, weakening the estimation of all unknowns, and deteriorating the positioning accuracy and stability (Nie et al., 2022). This may explain the reason that positioning accuracy at high-latitudes deteriorated more seriously than that in other regions due to the high CS occurrence rate.

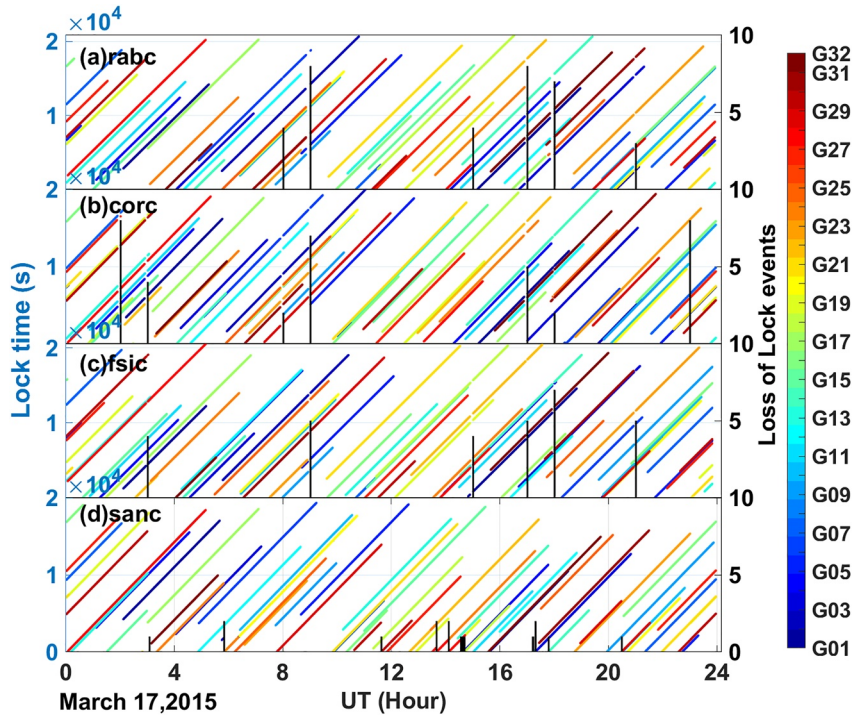

Figure 9. Satellite phase lock time on 17 March 2015 for four ISMRs from Canadian High Arctic Ionospheric Network. The vertical bar represents the number of the loss of lock events while the color bar on the right represent different satellites.

4.3. Cycle Slip Occurrence at High-Latitudes

Aimed at the problem proposed in Moreno et al., 2011 that large ROTI was observed simultaneously with positioning accuracy degradation for stations in the equatorial region, Zhang et al. (2014) found that the abnormal blunders and the failure of CS detection algorithms due to the high rate of TEC caused the positioning accuracy deterioration during ionospheric scintillation conditions. Although the characteristics of ionospheric scintillation in the equatorial and the polar region are different; for example, the amplitude scintillation favors in the equator while the phase scintillation favors in the polar region, the explanation for the significant accuracy degradation in Zhang et al. (2014) gave new insights for the positioning accuracy deterioration at high-latitudes. In fact, through several stations at high-latitudes, Juan, Sanz, González-Casado et al., 2018 reported that ionospheric fluctuations at high-latitudes usually do not produce CSs. Therefore, the key is to distinguish whether the detected CSs are true or false.

Fortunately, one additional advantage of the ISMRs used in this study is that they can provide the lock time of the signal. If the difference of the lock time is larger than the epoch interval, that is 60 s for the GPS Silicon Valley GSV4004B receiver in this study, it is regarded as the LoL event. By computing the number of the LoL events, we can infer the number of the actual CSs (Luo et al., 2019). The lock times for all GPS satellites at four selected ISMRs from CHAIN on 17 March 2015 are presented in Figure 9.

From Figure 9, we find that the total number of the LoL events for stations RABC, FSIC, CORC, and SANC were 34, 34, 36, and 36, respectively. However, under the default threshold of the PGF CS detector, the number of the CS satellites were 6,457, 6,513, 6,281, and 6,594, respectively. From the point view of using the LoL events to distinguish the actual CS, we can find that most of the CS satellites were falsely detected. In fact, when the threshold of the PGF observable increased to 0.5 m (Nie et al., 2022), the number of the CS satellites decreased to 87, 70, 85, and 339, respectively. Regarding that the epochs of the GPS observation were twice than that of the ISMR observation (the sampling rate of the GPS observations is 30 s while that of the ISMR observations is 60 s), the threshold of 0.5 m for the PGF observable is reasonable. The reasonability of the flexible threshold can also reflect from the kinematic positioning accuracy.

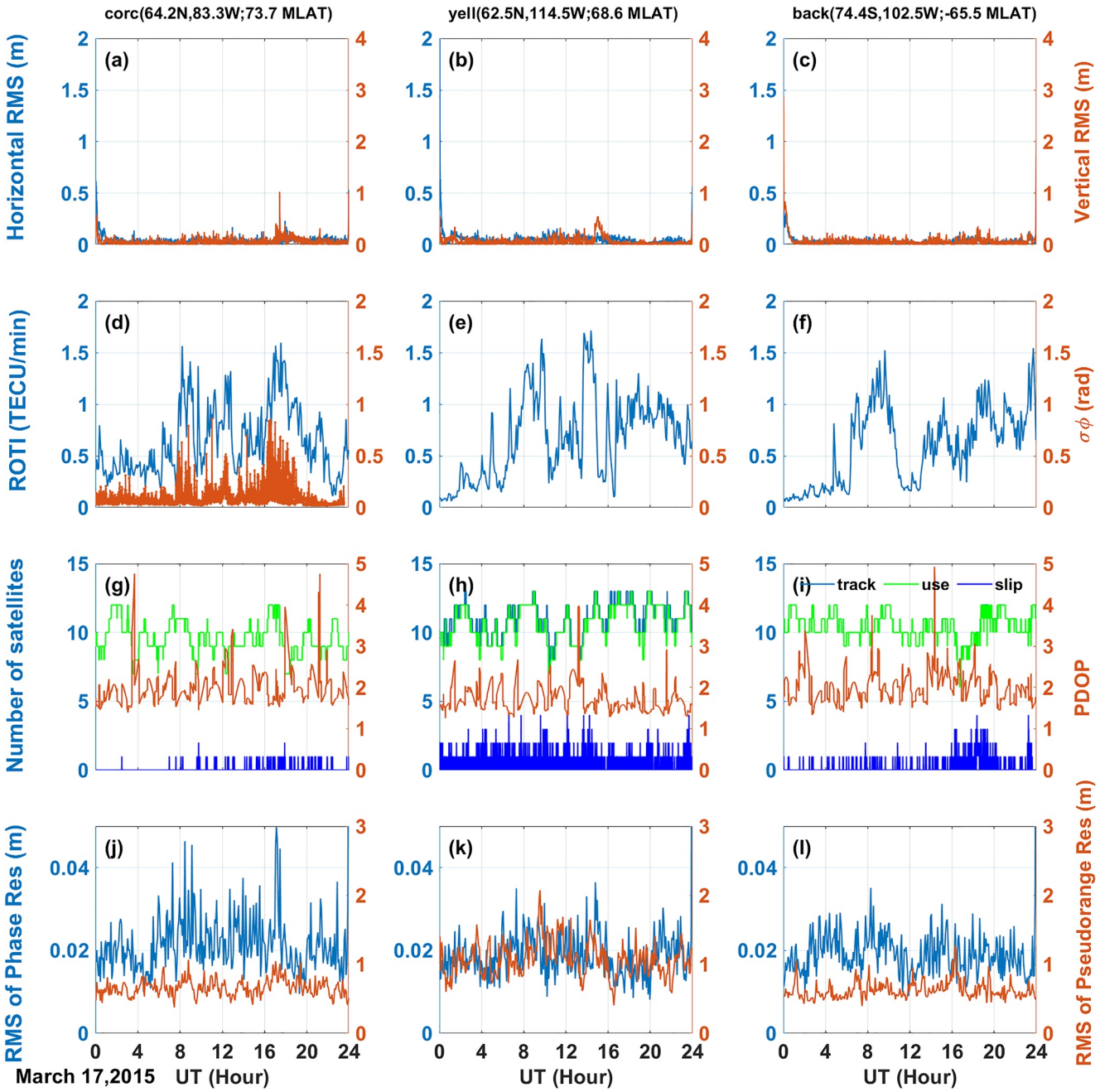

Figure 10. Same as Figure 7 but using a threshold of 0.5 m for the Phase-Geometry-Free cycle slip detector instead of the default threshold of 0.05 m.

From Figure 10, we can find that the positioning accuracy in the horizontal and vertical component for stations *CORC*, *YELL,* and *BACK* improved substantially compared to those presented in Figure 7. Using the threshold of 0.5 m for the PGF CS detector, the positioning accuracy in the horizontal and vertical component for the three stations were almost below 0.10 m, as shown in Figures 10(a)–10(c). As expected, we can see that the number of the CS satellites is substantially reduced, as shown in Figures 10(g)–10(i). With less satellites being flagged as CS, the kinematic PPP solution need not re-initialize the ambiguities; therefore, the positioning accuracy and stability are improved.

In order to confirm the applicability of the increased threshold, we reprocessed the 700 stations around the world. The 3D PPP errors on 17 March 2015 are presented in Figure 11 with the same arrangement than in Figure 5.

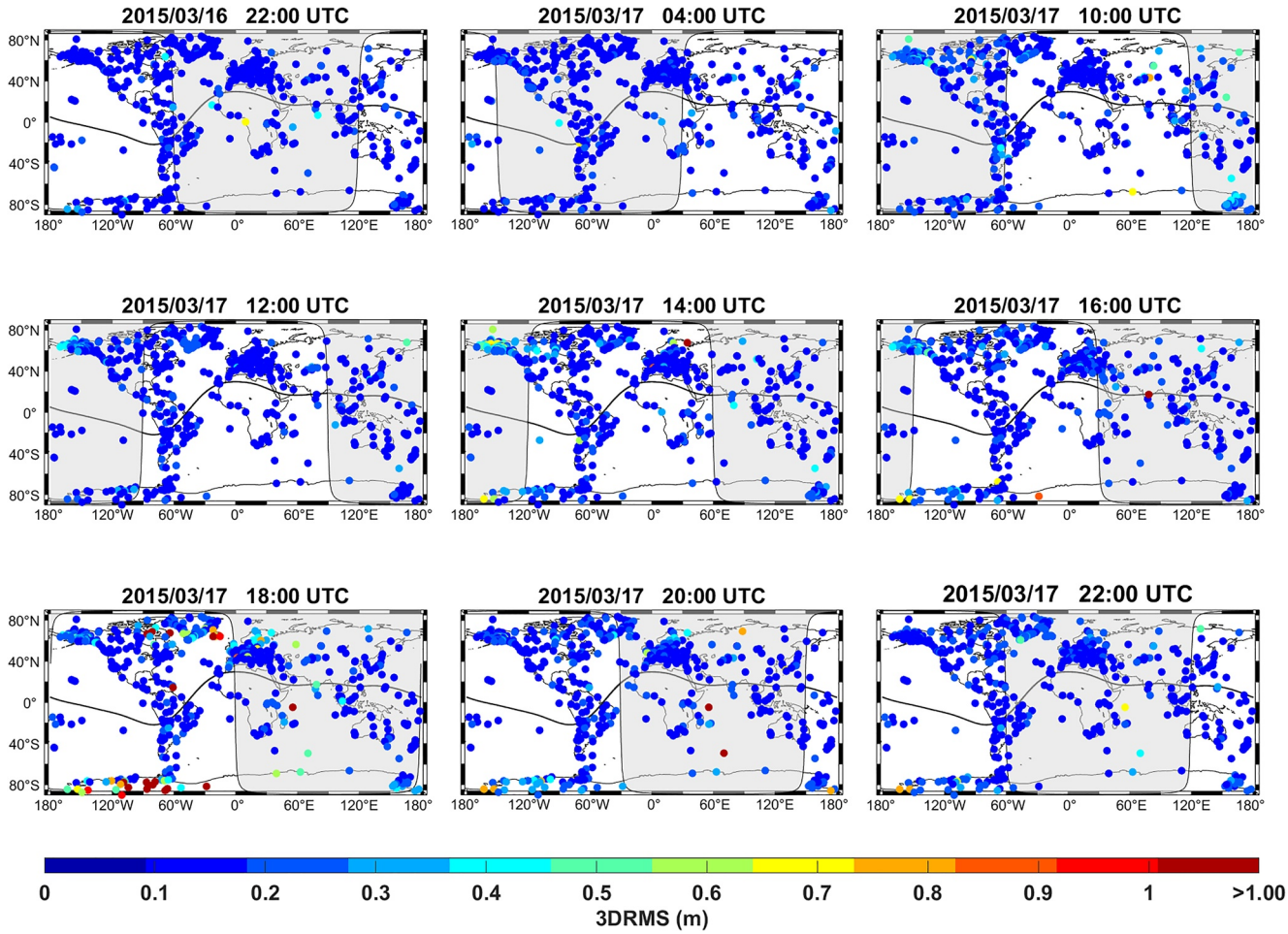

Figure 11. Same as Figure 5 but using a threshold of 0.5 m for the Phase-Geometry-Free cycle slip detector instead of the standard threshold of 0.05 m.

From Figure 11, we can find that most of the time, the 3D PPP errors for most of the stations were around 0.20 m. The exception was the time of 18:00 UT on 17 March 2015, when we found that the 3D positioning accuracy for some stations in the south hemisphere can still reach 1.0 m. The reason may be attributed to the inapplicability of the 0.5 m threshold of the PGF observable at that time. Comparing with Figure 5, we can find that the most significant improvement occurred at high-latitudes. In the same way, we quantified the horizontal and vertical positioning errors by separating the stations locating in high-, middle- and low-latitude region, as shown in Figure 12 and Table 3.

From Figure 12, we can see that both the horizontal and vertical errors for the different regions during the geomagnetic storm day of 17 March 2015 were almost the same magnitude as those during the geomagnetic quiet day of 16 March 2015.

5. Conclusions

The present study focuses on the kinematic PPP solution at high-latitudes on the most intense geomagnetic storm day of 17 March 2015. About 300 stations at high-latitudes were used in the experiment. In order to describe the ionospheric disturbance induced by the geomagnetic storm, the amplitude scintillation, phase scintillation, and ROTI metrics were exploited. We then evaluated the kinematic positioning performance at high-latitudes. In

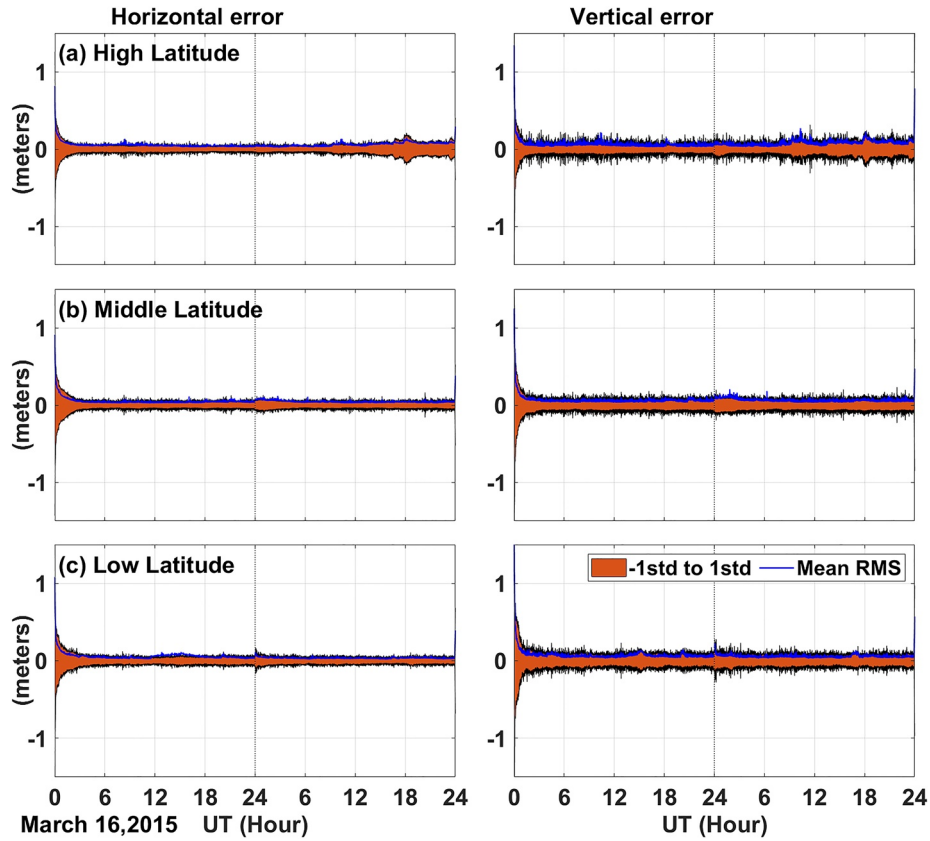

Figure 12. Same as Figure 6 but using the threshold of 0.5 m for the Phase-Geometry-Free cycle slip detector instead of the customary threshold of 0.05 m.

particular, we focus on the reason behind the significant positioning accuracy degradation at high-latitudes during the storm day. The major findings from our analysis are summarized as follows:

1. We observe that the phase scintillation was more severe than the amplitude scintillation at high-latitudes during the geomagnetic storm day. And the variation pattern of the ROTI was consistent with that of the phase scintillation indices.
2. During the geomagnetic storm, the kinematic PPP errors at high-latitudes were almost three times larger than those in the middle- and low-latitude regions. The large horizontal and vertical positioning errors at high-latitudes were accompanied by large ROTI values. From the perspective of GNSS data processing, the large positioning errors were also found to be related to the large number of the CS satellites.
3. Based on the lock time from ISMRs, we find that a large amount of the CSs was falsely detected under the conventional threshold for the PGF observable. By increasing the threshold, the kinematic PPP accuracy at high-latitudes can be improved to a similar magnitude as that at middle- and low-latitudes. The improved positioning accuracy may suggest that the ionospheric disturbance induced by the geomagnetic storm at high-latitudes has little effect on triggering actual CSs.

Table 3
Statistics of the Positioning Accuracy Under the Threshold of 0.5 m for the Phase-Geometry-Free Cycle Slip Detector in Different Regions on 17 March 2015

Geomagnetic latitude	Mean RMS (cm) 17 March 2015		Improvement	
	Horizontal	Vertical	Horizontal	Vertical
High	6.0	8.1	75.0%	77.6%
Middle	4.7	6.6	36.5%	34.0%
Low	3.8	6.0	44.1%	41.2%

CS detection is critical to achieve high accuracy and stability positioning performances during the disturbed ionospheric condition. It seems a good idea to tailor the threshold of the CS detector under the geomagnetic storm for stations at high-latitudes when actual CSs are not likely to occur. However, in the situation that there exists true CSs, increasing the threshold of the CS detector will also increase the risk of misdetection of the actual CSs that will degrade the positioning accuracy.

Data Availability Statement

The raw global positioning system data is provided by International GNSS Service (ftp://igs.ign.fr as well as https://cddis.nasa.gov/archive/), University NAVSTAR Consortium (https://data.unavco.org/archive/gnss/rinex/), and Canadian High Arctic Ionospheric Network (http://chain.physics.unb.ca/chain/). The Advanced Composition Explorer solar wind and interplanetary magnetic field data are provided from CDAWeb at https://cdaweb.gsfc.nasa.gov/. The longitudinally symmetric disturbances index in the horizontal direction H and Auroral Electrojet indices are provided by the Goddard Space Flight Center from https://omniweb.gsfc.nasa.gov/. The Real-Time Kinematic Library package (version 2.4.3 b34) for the positioning performances is retrieved from http://www.rtklib.com/.

Acknowledgments
The study is funded by the National Natural Science Foundation of China (No.42004012, 42004025), the Natural Science Foundation of Shandong Province, China (No.ZR2020QD048), the State Key Laboratory of Geo-Information Engineering (No.SKLGIE2019-Z-2-2), the State Key Laboratory of Geodesy and Earth's Dynamics (No. SKLGED-2021-3-4) and by the project RTI2018-094295-B-I00 funded by the MCIN/AEI 10.13039/501100011033, which is co-funded by the FEDER programme.

References

Afraimovich, E. L., Demyanov, V. V., & Kondakova, T. N. (2003). Degradation of GPS performance in geomagnetically disturbed conditions. *GPS Solutions*, *7*(2), 109–119. https://doi.org/10.1007/s10291-003-0053-7

Basu, S., Basu, S., MacKenzie, E., & Whitney, H. E. (1985). Morphology of phase and intensity scintillations in the auroral oval and polar cap. *Radio Science*, *20*(3), 347–356. https://doi.org/10.1029/RS020i003p00347

Basu, S., Groves, K., Basu, S., & Sultan, P. (2002). Specification and forecasting of scintillations in communication/navigation links: Current status and future plans. *Journal of Atmospheric and Solar-Terrestrial Physics*, *64*(16), 1745–1754. https://doi.org/10.1016/S1364-6826(02)00124-4

Bertiger, W., Bar-Sever, Y., Dorsey, A., Haines, B., Harvey, N., Hemberger, D., et al. (2020). GipsyX/RTGx, a new tool set for space geodetic operations and research. *Advances in Space Research*, *66*(3), 469–489. https://doi.org/10.1016/j.asr.2020.04.015

Blewitt, G. (1990). An automatic editing algorithm for GPS data. *Geophysical Research Letters*, *17*(3), 199–202.

Boehm, J., Niell, A. E., Tregoning, P., & Schuh, H. (2006). Global mapping function (gmf): A new empirical mapping function based on data from numerical weather model data. *Geophysical Research Letters*, *33*(7), L07304. https://doi.org/10.1029/2005GL025546

Cherniak, I., & Zakharenkova, I. (2015). Dependence of the high-latitude plasma irregularities on the auroral activity indices: A case study of 17 March 2015 geomagnetic storm. *Earth Planets and Space*, *67*(1), 151. https://doi.org/10.1186/s40623-015-0316-x

Cherniak, I., Zakharenkova, I., & Redmon, R. J. (2015). Dynamics of the high-latitude ionospheric irregularities during the 17 March 2015 St. Patrick's Day storm: Ground-based GPS measurements. *Space Weather*, *13*(9), 585–597. https://doi.org/10.1002/2015sw001237

Dach, R., Lutz, S., Walser, P., & Fridez, P. (2015). *Bernese GNSS software version 5.2*. University of Bern, Bern Open Publishing.

Förster, M., & Jakowski, N. (2000). Geomagnetic storm effects on the topside ionosphere and plasmasphere: A compact tutorial and new results. *Surveys in Geophysics*, *21*(1), 47–87.

Hatch, R. (1983). The synergism of GPS code and carrier measurements. *International geodetic symposium on satellite doppler positioning*.

Jacobsen, K. S., & Andalsvik, Y. L. (2016). Overview of the 2015 St. Patrick's day storm and its consequences for RTK and PPP positioning in Norway. *Journal of Space Weather and Space Climate*, *6*, A9. https://doi.org/10.1051/swsc/2016004

Jin, S., Jin, R., & Kutoglu, H. (2017). Positive and negative ionospheric responses to the March 2015 geomagnetic storm from BDS observations. *Journal of Geodesy*, *91*(6), 613–626. https://doi.org/10.1007/s00190-016-0988-4

Jin, Y., Spicher, A., Xiong, C., Clausen, L. B. N., Kervalishvili, G., Stolle, C., & Miloch, W. J. (2019). Ionospheric plasma irregularities characterized by the swarm satellites: Statistics at high latitudes. *Journal of Geophysical Research: Space Physics*, *124*(2), 1262–1282. https://doi.org/10.1029/2018ja026063

Juan, J. M., Sanz, J., González-Casado, G., Rovira-Garcia, A., Camps, A., Riba, J., et al. (2018). Feasibility of precise navigation in high and low latitude regions under scintillation conditions. *Journal of Space Weather and Space Climate*, *8*, A05. https://doi.org/10.1051/swsc/2018011

Juan, J. M., Sanz, J., Rovira-Garcia, A., González-Casado, G., Ibáñez, D., & Perez, R. O. (2018). AATR an ionospheric activity indicator specifically based on GNSS measurements. *Journal of Space Weather and Space Climate*, *8*, A14. https://doi.org/10.1051/swsc/2017044

Kamide, Y., McPherron, R., Gonzalez, W., Hamilton, D., Hudson, H., Joselyn, J., et al. (1997). *Magnetic storms: Current understanding and outstanding questions* (Vol. 98, pp. 1–19). Washington DC American Geophysical Union Geophysical Monograph Series. https://doi.org/10.1029/GM098p0001

Kintner, P., Ledvina, B., & De Paula, E. (2007). GPS and ionospheric scintillations. *Space Weather*, *5*(9). https://doi.org/10.1029/2006SW000260

Knight, M., & Finn, A. (1998). The effects of ionospheric scintillations on GPS. In *Proceedings of the 11th international technical meeting of the satellite division of the Institute of navigation* (pp. 673–685). Nashville, TN.

Liu, J., & Ge, M. (2003). PANDA software and its preliminary result of positioning and orbit determination. *Wuhan University Journal of Natural Sciences*, *8*(2), 603. https://doi.org/10.1007/BF02899825

Liu, J., Wang, W., Burns, A., Yue, X., Zhang, S., Zhang, Y., & Huang, C. (2016). Profiles of ionospheric storm-enhanced density during the 17 March 2015 great storm. *Journal of Geophysical Research: Space Physics*, *121*(1), 727–744. https://doi.org/10.1002/2015ja021832

Lu, Y., Wang, Z., Ji, S., & Chen, W. (2020). Assessing the positioning performance under the effects of strong ionospheric anomalies with multi-GNSS in Hong Kong. *Radio Science*, *55*(8). https://doi.org/10.1029/2019rs007004

Luo, X., Gu, S., Lou, Y., Chen, B., & Song, W. (2019). Better thresholds and weights to improve GNSS PPP under ionospheric scintillation activity at low latitudes. *GPS Solutions*, *24*(1). https://doi.org/10.1007/s10291-019-0924-1

Luo, X., Gu, S., Lou, Y., Xiong, C., Chen, B., & Jin, X. (2018). Assessing the performance of GPS precise point positioning under different geomagnetic storm conditions during solar cycle 24. *Sensors*, *18*(6), 1784. https://doi.org/10.3390/s18061784

Lyard, F., Lefevre, F., Letellier, T., & Francis, O. (2006). Modelling the global ocean tides: Modern insights from FES2004. *Ocean Dynamics*, *56*(5–6), 394–415.

Mansilla, G. A. (2019). Ionospheric disturbances at low and mid-low latitudes of the South American sector during the March 2015 great storm. *Advances in Space Research*, *63*(11), 3545–3557. https://doi.org/10.1016/j.asr.2019.02.009

McCaffrey, A. M., & Jayachandran, P. T. (2019). Determination of the refractive contribution to GPS phase "scintillation". *Journal of Geophysical Research: Space Physics*, *124*(2), 1454–1469. https://doi.org/10.1029/2018ja025759

Melbourne, W. (1985). The case for ranging in GPS-based geodetic systems. In *Proc. 1st int. symp. on precise positioning with GPS* (pp. 373–386).

Moreno, B., Radicella, S., De Lacy, M., Herraiz, M., & Rodriguez-Caderot, G. (2011). On the effects of the ionospheric disturbances on precise point positioning at equatorial latitudes. *GPS Solutions*, *15*(4), 381–390. https://doi.org/10.1007/s10291-010-0197-1

Nava, B., Rodríguez-Zuluaga, J., Alazo-Cuartas, K., Kashcheyev, A., Migoya-Orué, Y., Radicella, S. M., et al. (2016). Middle- and low-latitude ionosphere response to 2015 St. Patrick's Day geomagnetic storm. *Journal of Geophysical Research: Space Physics*, *121*(4), 3421–3438. https://doi.org/10.1002/2015ja022299

Nie, W., Wang, Y., Rovira-Garcia, A., Zheng, D., & Xu, T. (2022). Effect of the polar cap ionospheric sporadic-E layer on GNSS-based positioning: A case study at resolute bay, Canada, september 5, 2012. *GPS Solutions*, *26*(2), 60. https://doi.org/10.1007/s10291-022-01246-y

Petit, G., & Luzum, B. (2010). *IERS conventions (2010)*.

Pi, X., Mannucci, A., Lindqwister, U., & Ho, C. (1997). Monitoring of global ionospheric irregularities using the worldwide GPS network. *Geophysical Research Letters*, *24*(18), 2283–2286. https://doi.org/10.1029/97GL02273

Poniatowski, M., & Nykiel, G. (2020). Degradation of kinematic PPP of GNSS stations in central Europe caused by medium-scale traveling ionospheric disturbances during the St. Patrick's day 2015 geomagnetic storm. *Remote Sensing*, *12*(21), 3582. https://doi.org/10.3390/rs12213582

Prikryl, P., Ghoddousi-Fard, R., Weygand, J. M., Viljanen, A., Connors, M., Danskin, D. W., et al. (2016). GPS phase scintillation at high latitudes during the geomagnetic storm of 17–18 March 2015. *Journal of Geophysical Research: Space Physics*, *121*(10), 10448–10465. https://doi.org/10.1002/2016ja023171

Prikryl, P., Jayachandran, P., Mushini, S., Pokhotelov, D., MacDougall, J., Donovan, E., et al. (2010). GPS TEC, scintillation and cycle slips observed at high latitudes during solar minimum. *Annales Geophysicae*, *28*(6), 1307–1316. https://doi.org/10.5194/angeo-28-1307-2010

Prol, F. S., Kodikara, T., Hoque, M. M., & Borries, C. (2021). Global-scale ionospheric tomography during the March 17, 2015 geomagnetic storm. *Space Weather*, *19*(12). https://doi.org/10.1029/2021sw002889

Saastamoinen, J. (1972). Contributions to the theory of atmospheric refraction. *Bulletin Geodesique*, *105*(1), 279–298. https://doi.org/10.1007/BF02521844

Series, P. (2012). *Ionospheric propagation data and prediction methods required for the design of satellite services and systems* (pp. 531–613). Recommendation ITU-R.

Skone, S., Knudsen, K., & De Jong, M. (2001). Limitations in GPS receiver tracking performance under ionospheric scintillation conditions. *Physics and Chemistry of the Earth - Part A: Solid Earth and Geodesy*, *26*(6–8), 613–621. https://doi.org/10.1016/S1464-1895(01)00110-7

Skone, S., Lachapelle, G., Yao, D., Yu, W., & Watson, R. (2005). Investigating the impact of ionospheric scintillation using a GPS software receiver. In *Proceedings of the 18th international technical meeting of the satellite* (pp. 1126–1137). Division of The Institute of Navigation (ION GNSS 2005).

Sreeja, V., Aquino, M., & Elmas, Z. (2011). Impact of ionospheric scintillation on GNSS receiver tracking performance over Latin America: Introducing the concept of tracking jitter variance maps. *Space Weather*, *9*(10). https://doi.org/10.1029/2011SW000707

Sreeja, V. V., Aquino, M., Marques, H. A., & Moraes, A. (2020). Mitigation of ionospheric scintillation effects on GNSS precise point positioning (PPP) at low latitudes. *Journal of Geodesy*, *94*(2). https://doi.org/10.1007/s00190-020-01345-z

Takasu, T. (2013). *RTKLIB ver. 2.4. 2 manual. RTKLIB: An open source program package for GNSS positioning* (pp. 29–49).

Van Dierendonck, A. J., Klobuchar, J., & Hua, Q. (1993). Ionospheric scintillation monitoring using commercial single frequency C/A code receivers. *proceedings of ION GPS*, *93*, 1333–1342.

Wubbena, G. (1985). Software developments for geodetic positioning with GPS using TI 4100 code and carrier measurements. *Proceedings 1st international symposium on precise positioning with the global positioning system*, 403–412.

Yang, Z., Morton, Y. T. J., Zakharenkova, I., Cherniak, I., Song, S., & Li, W. (2020). Global view of ionospheric disturbance impacts on kinematic GPS positioning solutions during the 2015 St. Patrick's day storm. *Journal of Geophysical Research: Space Physics*, *125*(7). https://doi.org/10.1029/2019ja027681

Yao, Y., Liu, L., Kong, J., & Zhai, C. (2016). Analysis of the global ionospheric disturbances of the March 2015 great storm. *Journal of Geophysical Research: Space Physics*, *121*(12), 12157–12170. https://doi.org/10.1002/2016JA023352

Zakharenkova, I., Astafyeva, E., & Cherniak, I. (2016). GPS and GLONASS observations of large-scale traveling ionospheric disturbances during the 2015 St. Patrick's Day storm. *Journal of Geophysical Research: Space Physics*, *121*(12), 12138–12156. https://doi.org/10.1002/2016ja023332

Zakharenkova, I., & Cherniak, I. (2021). Effects of storm-induced equatorial plasma bubbles on GPS-based kinematic positioning at equatorial and middle latitudes during the September 7–8, 2017, geomagnetic storm. *GPS Solutions*, *25*(4). https://doi.org/10.1007/s10291-021-01166-3

Zakharenkova, I., Cherniak, I., & Krankowski, A. (2019). Features of storm-induced ionospheric irregularities from ground-based and spaceborne GPS observations during the 2015 St. Patrick's day storm. *Journal of Geophysical Research: Space Physics*, *124*(12), 10728–10748. https://doi.org/10.1029/2019ja026782

Zhang, X., Guo, F., & Zhou, P. (2014). Improved precise point positioning in the presence of ionospheric scintillation. *GPS Solutions*, *18*(1), 51–60. https://doi.org/10.1007/s10291-012-0309-1